A Close-up Look at Electronic Spectroscopic Signatures of Common Pharmaceuticals in Solution

Sara Gómez, Matteo Ambrosetti,[a] Tommaso Giovannini, and Chiara Cappelli*

Scuola Normale Superiore, Classe di Scienze, Piazza dei Cavalieri 7, 56126, Pisa, Italy

E-mail: chiara.cappelli@sns.it

[a]Current affiliation: Northvolt AB, Sweden

Abstract

Simulating electronic properties and spectral signals requires robust computational approaches that need tuning with the system's peculiarities. In this paper, we test implicit and fully atomistic solvation models for the calculation of UV-Vis and Electronic Circular Dichroism (ECD) spectra of two pharmaceutically relevant molecules, namely, (2S)-Captopril and (S)-Naproxen, dissolved in aqueous solution. Room temperature molecular dynamics (MD) simulations reveal that these two drugs establish strong contacts with the surrounding solvent molecules via hydrogen bonds. Such specific interactions, which play a major role in the spectral response and are neglected in implicit approaches, are further characterized and quantified with Natural Bond Orbitals (NBO) methods. Our calculations show that simulated spectra, and especially ECD, are in good agreement with experiments solely when conformational and configurational dynamics, mutual polarization, and solute-solvent repulsion effects are considered.

1 Introduction

The study of electronic transitions and excited states of molecules has a wealth and long story that involves different experimental and computational methodologies. In that field, two well-known techniques are UV-Vis absorption and Electronic Circular Dichroism (ECD) spectroscopies.[1–3] ECD is a chiroptical spectroscopy that measures the difference between the absorption coefficients for left and right circularly polarized light. Like other chiroptical spectroscopies,[4–7] its ultimate goal is thus to determine the absolute configuration of chiral substances.[8,9] For this reason, ECD finds applications in the characterization of the secondary structure of biopolymers, such as peptides and nucleic acids, and in determining the absolute configuration of compounds with pharmacological relevance.[10–12] ECD intensities are associated with rotatory strengths that are related to electric and magnetic transition moments.[1] Due to the different absorption of left/right polarized light, ECD signals can be positive or negative. This feature adds an extra "dimension" to the spectra compared to the dimensionality of traditional UV-Vis spectroscopy, making ECD spectroscopy extremely sensitive to the specificity of molecules' geometric and electronic structures.[13]

Electronic structure calculations can serve as a tool to both interpret experimental spectra and predict ECD profiles when measurements are not available.[4] The assignment of absolute configurations of chiral systems by computed ECD spectra can be accurately achieved if validated computational protocols are used.[14–17] These protocols need to account for an accurate description of solvent effects on spectral signal since the large majority of experiments are performed in the condensed phase.[18] In particular, solvent effects can be crucial in determining the ECD spectral profile, especially when specific, strong, and directional interactions, such as Hydrogen Bonds (HB), are present. This is the case of aqueous solutions, which are the natural environment for biological systems. To deal with the specificities of such an environment, fully atomistic Quantum Mechanics/Molecular Mechanics (QM/MM) approaches can be used.[19,20] There, the chiral molecule is treated at the QM

level, whereas the solvent is atomistically described by means of classical mechanics. The most accurate approaches belong to the family of polarizable QM/MM methods, where the QM part can polarize the MM region and vice-versa, in a mutual polarization fashion.[21] Among the many polarizable QM/MM methods,[17,19,22–25] QM/Fluctuating Charges (QM/FQ)[24] and QM/Fluctuating Charges and Fluctuating Dipoles (QM/FQFμ)[26–28] have extensively proved to yield a reliable description of spectral signals of systems dissolved in aqueous solution.[21,29,30]

In polarizable QM/MM methods, the QM/MM interaction is limited to electrostatics and polarization terms. However, even for polar solvents such as water, non-electrostatic interactions can be relevant.[31–35] For this reason, in this work we refine the modeling of QM/MM interactions so as to include quantum confinement effects (Pauli repulsion) in the evaluation of spectral signals and electronic properties. This is achieved by exploiting an approach explicitly dependent on the QM density, which we have recently developed and that is general enough to be coupled to any QM/MM method.[36]

In this work, QM/FQ and QM/FQFμ are challenged to simulate the UV-Vis and ECD spectra of two well-known chiral molecules (2S)-1-[(2S)-2-methyl-3-sulfanylpropanoyl]pyrrolidine-2-carboxylic acid – Captopril – and (+)-(S)-2-(6-Methoxynaphthalen-2-yl)propanoic acid – Naproxen – (CAP and NAP in what follows) when dissolved in aqueous solution. Both drugs are employed in clinical and pharmaceutical settings as pure (S,S) and (S) epimers, which are responsible for the angiotensin-converting enzyme (ACE) inhibitory and anti-inflammatory action, respectively.[37–39] To the best of our knowledge, this is the first work where solvent effects on the ECD spectra of solvated CAP and NAP are assessed.

The paper is organized as follows: in the next section, the theoretical and computational fundamentals are briefly reviewed. After a short discussion on the computational protocol, UV-Vis and ECD results obtained for CAP and NAP in aqueous solution are presented and compared to the experimental spectra. Conclusions and future perspectives close the manuscript.

2 Short theoretical background

Within the polarizable QM/FQ model, each MM atom is endowed with a polarizable charge that varies as a response to the QM electrostatic potential and the differences in the electronegativity between each MM atom. QM/FQFμ model is a pragmatical extension of QM/FQ, which additionally endows each MM atom with a polarizable dipole. In this way, the anisotropy of specific interactions, such as HB, can be considered. The QM density interacts with charges in case of QM/FQ, with both charges and dipoles in QM/FQFμ. For a self-consistent-field (SCF) method, the total QM/FQFμ energy ($\mathcal{E}$) and the effective Fock matrix ($\tilde{F}_{\mu\nu}$) expressed in the Atomic Orbitals (AO) basis set $\{\chi_\mu\}$ read:

$$\begin{aligned}\mathcal{E}(\mathbf{D},\mathbf{q},\boldsymbol{\mu},\boldsymbol{\lambda}) = \text{tr } \mathbf{hD} + \frac{\mathbf{1}}{\mathbf{2}}\text{tr } \mathbf{DG(D)} + \frac{\mathbf{1}}{\mathbf{2}}\mathbf{q}^\dagger\mathbf{T}^{\mathbf{qq}}\mathbf{q} + \frac{\mathbf{1}}{\mathbf{2}}\boldsymbol{\mu}^\dagger\mathbf{T}^{\mu\mu}\boldsymbol{\mu} + \\ + \mathbf{q}^\dagger\mathbf{T}^{q\mu}\boldsymbol{\mu} + \boldsymbol{\chi}^\dagger\mathbf{q} + \boldsymbol{\lambda}^\dagger\mathbf{q} + \mathbf{q}^\dagger\mathbf{V(D)} - \boldsymbol{\mu}^\dagger\mathbf{E(D)} \end{aligned} \quad (1)$$

$$\tilde{F}_{\mu\nu} = \frac{\partial\mathcal{E}}{\partial D_{\mu\nu}} = h_{\mu\nu} + G_{\mu\nu}(\mathbf{D}) + \mathbf{V}^\dagger_{\mu\nu}\mathbf{q} - \mathbf{E}^\dagger_{\mu\nu}\boldsymbol{\mu} \quad (2)$$

where $\mathbf{h}$ and $\mathbf{G}$ are the one- and two-electron matrices, and $\mathbf{D}$ is the density matrix. $\boldsymbol{\chi}$ gathers atomic electronegativities, while T^{qq}_{ij}, $\mathbf{T}^{q\mu}_{ij}$ and $\mathbf{T}^{\mu\mu}_{ij}$ are charge-charge, charge-dipole and dipole-dipole interaction kernels, respectively. Their expressions can be found in Refs. 26,40. $\mathbf{q}^\dagger\mathbf{V(D)}$ and $\boldsymbol{\mu}^\dagger\mathbf{E(D)}$ terms describe the electrostatic interactions between the QM density and the FQs and Fμs, respectively. $\boldsymbol{\lambda}$ is a set of Lagrangian multipliers that impose specific charge constraints on each molecule.[26]

To feed Eq. 2, charges and dipoles are computed by imposing the global functional to be stationary with respect to charges, dipoles, and Lagrangian multipliers. Such procedure

leads to the following linear system:[26]

$$\left(\begin{array}{ccc|c} \mathbf{T}^{qq} & \mathbf{1}_{\boldsymbol{\lambda}} & \mathbf{T}^{q\mu} & \\ \mathbf{1}_{\boldsymbol{\lambda}}^{\dagger} & \mathbf{0} & \mathbf{0} & \\ \hline -\mathbf{T}^{q\mu^{\dagger}} & \mathbf{0} & \mathbf{T}^{\mu\mu} & \end{array}\right)\left(\begin{array}{c} \mathbf{q} \\ \boldsymbol{\lambda} \\ \hline \boldsymbol{\mu} \end{array}\right) = \left(\begin{array}{c} -\boldsymbol{\chi} \\ \mathbf{Q}_{\mathrm{tot}} \\ \hline \mathbf{0} \end{array}\right) + \left(\begin{array}{c} -\mathbf{V}(\mathbf{D}) \\ \mathbf{0} \\ \hline \mathbf{E}(\mathbf{D}) \end{array}\right) \tag{3}$$

$$\mathbf{M}\mathbf{L}_{\lambda} = -\mathbf{C}_{Q} - \mathbf{R}(\mathbf{D}) \tag{4}$$

where $\mathbf{1}_{\lambda}$ accounts for the Lagrangian blocks, $\mathbf{C}_{Q}$ collects atomic electronegativities and charge constraints. $\mathbf{L}_{\lambda}$ is the vector containing charges, dipoles, and Lagrangian multipliers, and $\mathbf{R}(\mathbf{D})$ represents the QM potential and field. QM/FQ equations are easily recovered by discarding all terms depending on μ in Eqs. 1 and 2 and by discarding rows/columns involving μs and their response in Eq. 3.

To include Pauli repulsion contributions we exploit the approach presented in Ref. 31. This model consists of building a mimicked density for the MM portion of the system (ρ_{MM}). This is achieved by localizing fictitious valence electron pairs for the MM molecules in their bond and lone pair regions and representing them by s-gaussian-type functions.[36] The Pauli repulsion energy term is then computed as the following (opposite) exchange integral:

$$E_{rep} = \int \frac{\rho_{\mathrm{QM}}(\mathbf{r}, \mathbf{r}')\rho_{\mathrm{MM}}(\mathbf{r}', \mathbf{r})}{|\mathbf{r} - \mathbf{r}'|}\, \mathrm{d}\mathbf{r}\, \mathrm{d}\mathbf{r}' \tag{5}$$

Differently from parametric formulations (e.g., LJ potential) that do not modify the Hamiltonian, Eq. 5 explicitly depends on the QM density and thus directly contributes to the Fock matrix. In this way, an indirect contribution to all sets of excited state properties is obtained.[41]

With the purpose of computing UV-Vis and ECD spectra, we use Time-dependent density functional theory (TD-DFT).[42] In the framework of QM/FQ(Fμ), the embedding-dependent terms arising from the polarizable environment must be included in the response operator, ultimately adding extra terms in the $\tilde{A}$ and $\tilde{B}$ matrices of Casida's equations.[43] We refer

the interested readers to Refs. 27,41 for further details. The inclusion of QM/MM quantum repulsion instead does not add extra terms to Casida's equations because they act as a one-electron contribution to the Fock matrix (see Eq 5).[33]

Electronic excitation energies and the electric and magnetic transition dipole moments can be obtained from the eigenvalues and eigenvectors of the response equations, respectively. These quantities allow the calculation of UV/Vis and ECD spectra, by using the oscillator strength f_{n0}, and ECD rotatory strength, R_{n0} for each excitation from the ground state Ψ_0 to the nth excited state Ψ_n, $0 \rightarrow n$ (in a.u.):[44]

$$f_{n0} = \frac{2\omega_{n0}}{3} \sum_{\alpha=x,y,z} |\langle \Psi_0 | \hat{\mu}_\alpha | \Psi_n \rangle|^2 \tag{6}$$

$$R_{n0} = \mathrm{Im} \langle \Psi_0 | \hat{\mu} | \Psi_\mathrm{n} \rangle \langle \Psi_\mathrm{n} | \hat{\mathrm{m}} | \Psi_0 \rangle$$

$$R_{n0}^{(v)} = \sum_{\alpha=x,y,z} \frac{1}{\omega_{n0}} \mathrm{Im} \langle \Psi_0 | \hat{\mathrm{p}_\alpha} | \Psi_\mathrm{n} \rangle \langle \Psi_\mathrm{n} | \hat{\mathrm{m}} | \Psi_0 \rangle \tag{7}$$

where Ψ_0 and Ψ_n are the wavefunctions, $\hat{\mu}$ and $\hat{m}$ are the electric and magnetic dipole operators, ω_{n0} is the transition energy. In the above notation, $R_{n0}^{(v)}$ means that the rotatory strength is evaluated in the velocity gauge.

3 Methods

QM/MM calculations of both UV-Vis and ECD spectra are performed by relying on the following multi-step protocol:[21]

1. **Definition of the system**: the molecular system is composed of the target molecule (solute, here NAP or CAP) and its surrounding environment (solvent, here water). Using Marvin Beans version 19.20,,[45] a preliminary investigation of protonation states as a function of pH is conducted. The speciation plots show that at neutral pH (pH=7.0) CAP and NAP stay in anionic forms, with deprotonated carboxylic groups. Their

structures are depicted in Figs. 1a and 1b, respectively.

Initial geometries of both drugs are adapted from the Protein Data Bank (PDB), specifically from coordinates associated with residues called X8Z and NPS, respectively.[46,47] Relaxed scans around the principal dihedral angles of CAP and NAP ($\delta 1$, $\delta 2$, and $\delta 3$ in Fig. 1) are performed at the CAM-B3LYP/aug-cc-pVDZ level of theory, and the structures of the resulting conformers are optimized at the same level. In those steps, aqueous solvent effects are included by means of the Polarizable Continuum Model.[48]

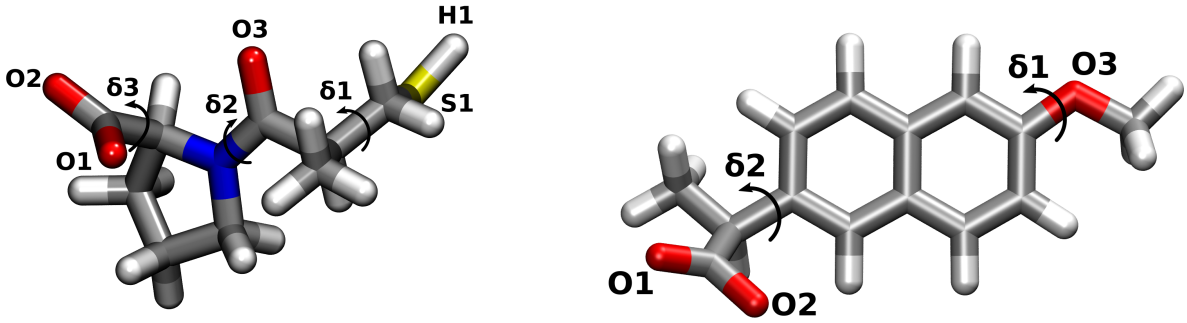

a. (2S)-Captopril b. (S)-Naproxen

Figure 1: Anionic CAP (left) and NAP (right) molecular structures. Selected atom labels and dihedral angles are highlighted.

2. **Classical Molecular Dynamics (MD) simulation**: an MD simulation is performed for each molecule (CAP or NAP) surrounded by water molecules. MD runs are sufficiently long to sample the phase space. Force field parametrizations for the solutes are generated by relying on the ANTECHAMBER package and the general Amber force field (GAFF).[49,50] To refine electrostatic solute-solvent interactions, the solute charges are computed by exploiting the multiconformational RESP (MultiRESP) procedure.[51] Each drug molecule is then placed in the center of a cubic box with an edge of 60 Å and surrounded by roughly 7700 TIP3P-FB[52] water molecules. To neutralize the net charge of the system, a sodium counterion is placed in the simulation cell.

   Systems composed of the flexible anionic solute and the water molecules are minimized using the steepest descent algorithm until the force on each atom results lower than

1000.0 kJ/mol/nm. Two subsequent equilibration steps are performed before the production run. In the first one, which lasts 1.0 ns and is conducted in the NVT ensemble, the system is slowly heated from 0 to 298.15 K. The 2.0 ns second equilibration step is then performed in the NPT ensemble. A velocity rescaling including a stochastic term,[53] with time constants of 0.1 ps, is used to control the temperature, whereas a Parrinello-Rahman barostat,[54] with a time constant of 2.0 ps, is used to control the pressure of the system. Periodic boundary conditions are applied in all directions. VdW forces are computed using a cutoff distance of 12 Å. Long-range electrostatic interactions are treated with the Particle Mesh Ewald (PME) method,[55,56] using a real-space cutoff radius of 12 Å. 50 ns production runs are performed in the NPT ensemble at 298.15 K. A time step of 2.0 fs is adopted for all the MD steps. The LINCS[57,58] algorithm is used in order to freeze the fastest internal degrees of freedom, i.e., hydrogen atoms. System coordinates are stored for every 2.0 ps of simulation. All molecular simulations are carried out with the GROMACS 2020.3 package.[59–64]

3. **Definition of the different regions of the two-layer scheme**: Different sets (from 100 to 1100) of uncorrelated snapshots are extracted from the last 40 ns of the MD runs. For each snapshot, a sphere centered on the center of mass of the drug is cut, with radii of 17 and 20 Å for CAP and NAP, respectively, so as to retain all relevant solute-solvent interactions. Such cutoffs are chosen based on the information provided by the Radial Distribution Functions (RDF) retrieved from the MD trajectories through the TRAVIS package.[65,66] The diverse sets of snapshots serve to evaluate convergence for the studied properties.

4. **QM/MM calculations**: For each snapshot, UV-Vis and ECD spectra are calculated by exploiting three different QM/MM approaches (QM/TIP3P, QM/FQ, and QM/FQFμ) where the drug is the only included in the QM portion and is treated at the CAM-B3LYP/aug-cc-pVDZ level. In the case of QM/FQ, two different parametriza-

tions are exploited (QM/FQ^a from Ref 67 and QM/FQ^b from Ref 32). In addition to the purely electrostatic (and polarizable) QM/MM interactions, solute-solvent Pauli repulsion is considered by following the approach reported in Ref. 31. For the sake of comparison, vacuum and QM/PCM UV-Vis and ECD spectra are also computed. The first 20 excited states are considered in all TD-DFT calculations. Canonical Molecular Orbitals (CMO) analysis, as implemented in NBO,[68–70] is used to assign the orbitals involved in the main transitions.[71–73] Further NBO calculations, in particular, stabilization energies, are carried out to identify and quantify the strongest target-environment interactions after expanding the QM region to include the first solvation shell of each drug, i. e., the water molecules in the closest contact (2.3 Å) with the drug.

5. **Extraction of the averaged spectra (see Eq. 7) and analysis of the results:** Raw UV-Vis and ECD data obtained from each snapshot are convoluted with a Gaussian function, with a full width at half maximum (FWHM) of 0.25 eV. Then, the individual spectra are averaged to obtain the final ones, which are compared with their experimental data.

Calculations are performed using a locally modified version of the Gaussian16 package.[74] Interaction energies are obtained via second-order perturbation corrections to the Fock matrix with the NBO7 program.[75]

4 Results

This section reports the results obtained on UV-Vis and ECD spectra of solvated CAP and NAP. To analyze solvent effects, spectra are simulated by a variety of models: the implicit Polarizable Continuum Model (PCM),[48] an electrostatic embedding approach (QM/TIP3P),[76] and the polarizable QM/FQ and QM/FQFμ models, with and without an explicit description of Pauli repulsion effects. Note that QM/FQFμ is here applied for the first time to compute ECD spectra in a solvent. Computed results are compared with measured UV-Vis and ECD

spectra. In addition, the hydrogen bonding and strength of specific solute-solvent interactions are quantified using Natural Bond Orbitals (NBO) methods to provide a rationale for our findings.[69,70]

4.1 (2S)-Captopril

4.1.1 Conformational sampling and MD analysis

Due to its significance as a potent ACE inhibitor, an extensive conformational search of captopril has already been reported,[77,78] in its neutral and double anionic forms, evaluating the effect of the solvent[37] via the conductor-like PCM (CPCM).[79] Apart from the conventional conformational changes, cis-trans isomerization processes can also happen to CAP.[78] Our conformational search, initially assessed by exploiting the implicit PCM model at the CAM-B3LYP/aug-cc-pVDZ level of theory, leads to four minima according to the scans reported in Fig. S1 in the Supporting Information (SI). The highest QM/PCM rotational barrier is more than 25 kcal/mol for the rotation of the proline group of the drug, $\delta 2$ in Fig. 1a. Other rotations do not exceed 5 kcal/mol in their barriers, confirming the flexibility of the molecule. Combined dihedral distribution functions (DDF) for the main angles and CAP equilibrium structures are displayed in Fig. 2. Diverse dihedral angle values are sampled, overcoming the rotational barriers in the $\delta 2$ case. Notice that the structure **C** is the most sampled conformation during the MD runs, even if the lowest-energy minimum (Structure **A** in Fig. 2) serves as the starting point in the MD sampling. The four motifs are used to perform QM/PCM calculations.

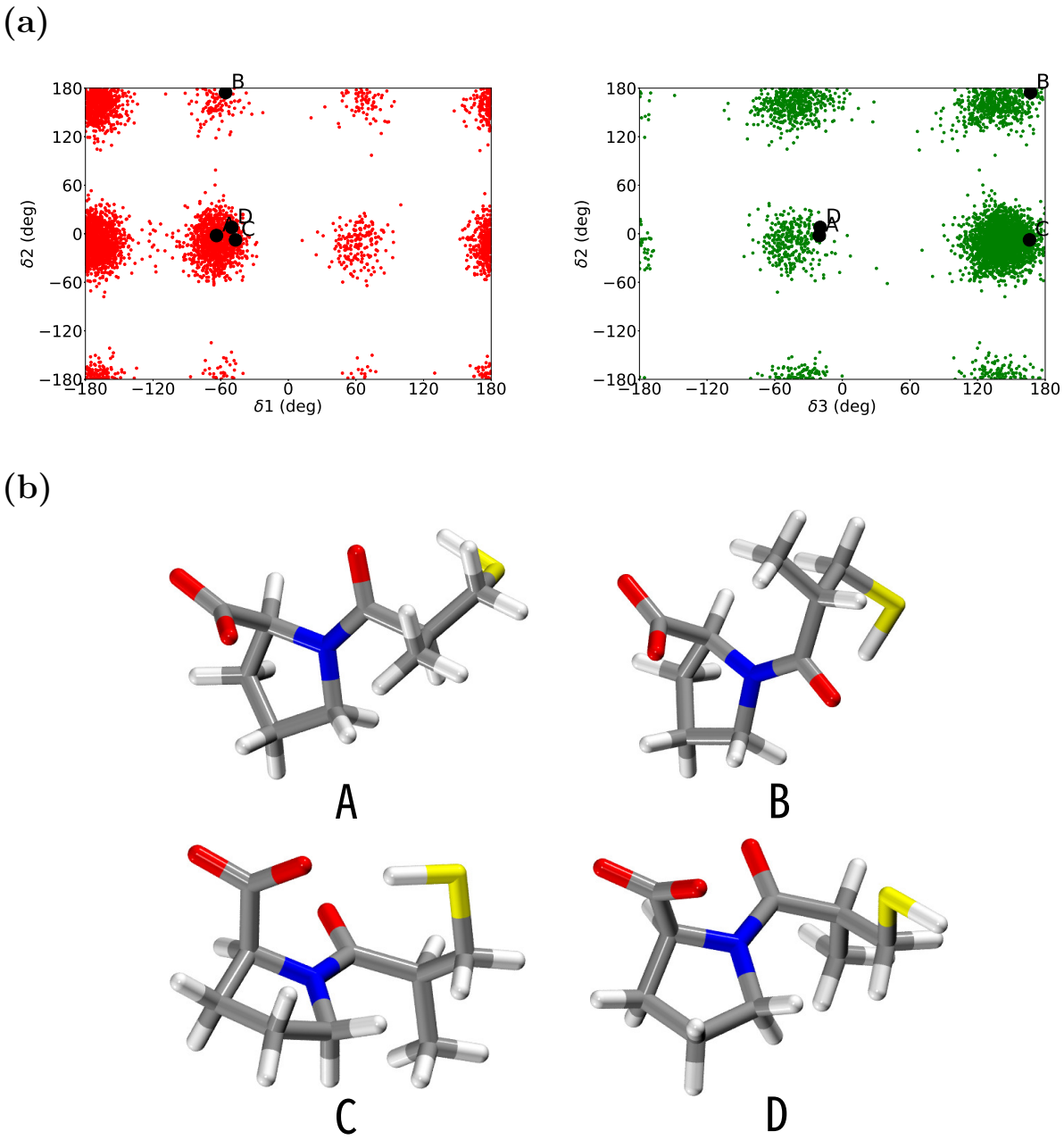

Figure 2: (a) CAP combined dihedral distribution functions for selected angles (see Fig. 1a). (b) CAP conformers obtained from dihedral scans.

In order to analyze the hydrogen-bonding patterns between the QM molecule and its surrounding environment, i.e., the water molecules, RDFs, and the corresponding running coordination numbers (RCN) computed as the integral of the RDF up to its first/second minimum for any specific atom, are calculated and reported in Fig. 3. The three oxygen (O1, O2, O3), the sulfur (S1), and the sulfur-linked hydrogen (H1) atoms are considered

(see Fig. 1a for atom labeling) as potential HB sites with the solvent. The two well-defined peaks at about 1.75 Å for the carbonyl and carboxylate oxygen atoms indicate a strong HB interaction between CAP and the near water molecules. RCNs vary from approximately 3.0 for carboxylate O1 and O2 to 2.0 for the carbonyl O3, showing, as expected, a slight preferential HB interaction with the charged group. In contrast, for solvent interactions via the thiol group of CAP, peaks at longer distances, 2.1 (H1) and 2.2 (S1) Å emerge and give rise to RCNs of less than 1.0. The above analysis leads to having, on average, seven water molecules in the closest vicinity of CAP when it is solvated.

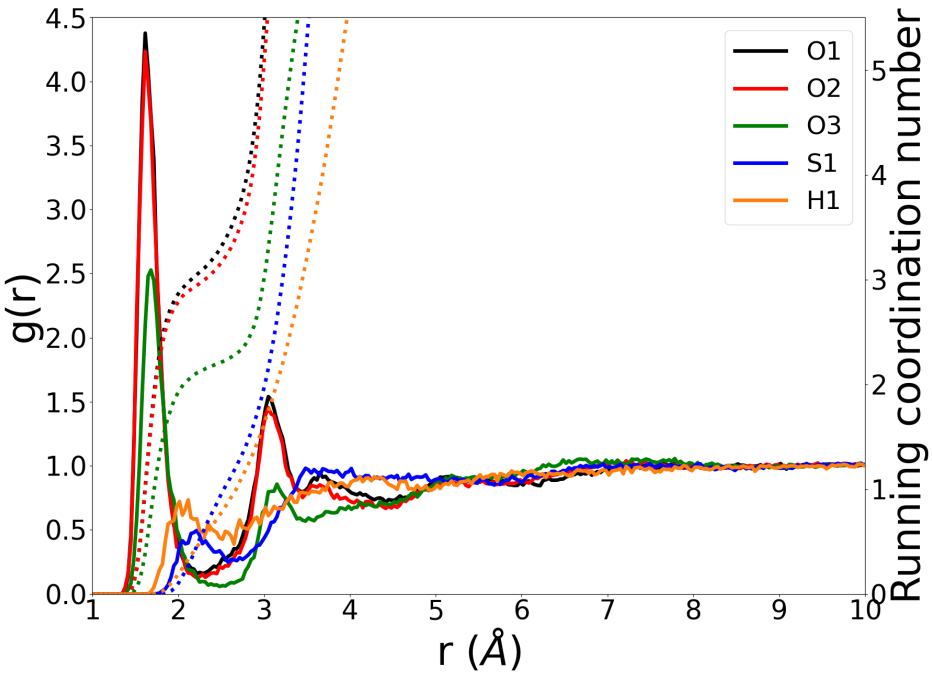

Figure 3: Radial distribution function (continue lines) and running coordination number (dotted lines) of CAP in water. Labels are reported in Fig. 1a.

4.1.2 UV-Vis Absorption Spectrum

As an example of the spectral profile building, QM/FQFμ UV-Vis and ECD spectra are plotted in Fig. 4 together with the raw data (reported as grey sticks) extracted from each snapshot. Sticks-like spectra for the other approaches are deposited in the SI, Figs. S3 and S4. It is worth mentioning that QM/MM final spectra originate from averaging the

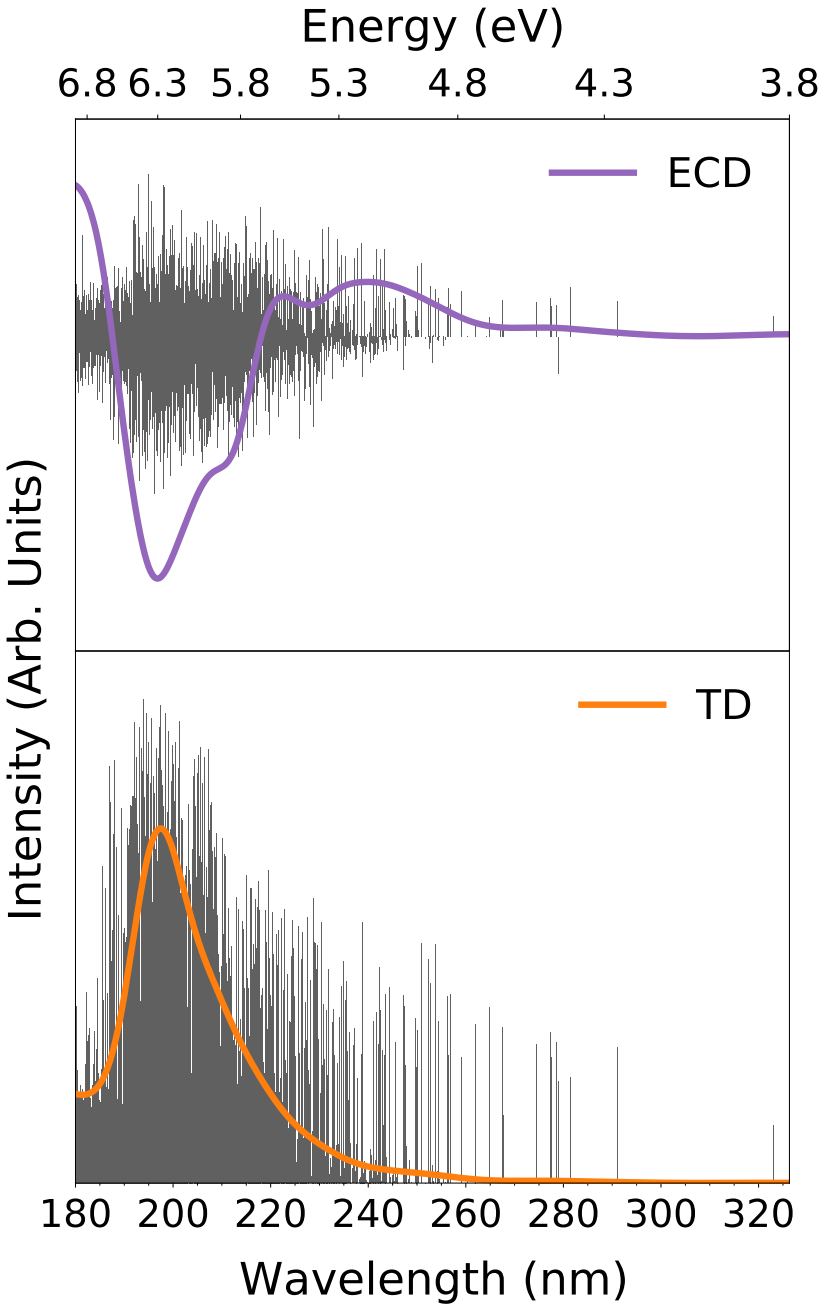

Figure 4: QM/FQFμ ECD (top) and UV-Vis (bottom) raw stick and convoluted spectra of CAP in aqueous solution, computed at the CAM-B3LYP/aug-cc-pVDZ level of theory. Gaussian functions with an FWHM of 0.25 eV are used in the convolution. Total frames: 900

individual convoluted results over 600 uncorrelated snapshots extracted from the MD run. The convergence of QM/MM computed spectra has carefully been examined by considering an increasing number of snapshots (see Figs. S5-S6 in the SI).

The first observation from the sticks in Fig. S3 in the SI is that in the 150-350 nm range, the UV-Vis spectrum of CAP in water is characterized by two main bands regardless of the exploited QM/MM approach. However, from 180 nm on, the lowest experimental reported limit, just a single well-defined band appears (see Fig. 4). Another important thing is that each QM/MM approach shows a peculiar spread of sticks both in energy/wavelengths and intensities. This can be particularly appreciated by considering the larger spread reported by QM/FQ^b (and QM/FQFμ) with respect to QM/FQ^a, and indeed, it confirms that there is a different description of solute-solvent electrostatic (polarizable) interactions when exploiting diverse models and/or parametrizations. Remarkably, QM/FQ^b and QM/FQFμ spectra are almost identical, thus showing that the anisotropic contributions arising from the inclusion of Fμs are negligible in this case.

Convoluted UV-Vis spectra with the diverse approaches used in this work are shown in Fig. 5, along with the experimental spectrum.[80] The experimental UV-Vis absorption spectrum of CAP consists of a single band exhibiting a maximum at 205 nm.[80] Computations in the gas phase yield a very displaced band with respect to the experiment, while all the approaches that are here exploited to include solvent effects improve the computed spectrum. Table S2 in the SI lists wavelengths for CAP (also for NAP) maximum absorption energies calculated by means of the various solvation approaches. All spectra computed with any of the QM/MM methods are blueshifted with respect to the experiment. Among them, the QM/FQ^a embedding approach reproduces better the experimental data, placing the maximum at 200.7 nm. Regarding the inclusion of repulsion, there are no significant changes in simulated spectra, and just in the case of QM/FQ^b and QM/FQFμ methods, a slight shift (< 2 nm) can be appreciated. On the basis of the CMO decomposition, the transition that leads to the emergence of the main band has a $\pi \rightarrow \pi^*$ nature and involves the amidic $\pi_{\mathrm{C{=}O3{+}N}}$ and $\pi^*_{\mathrm{C{=}O3}}$ orbitals (graphically depicted in Fig. 5) regardless of the solvation model.

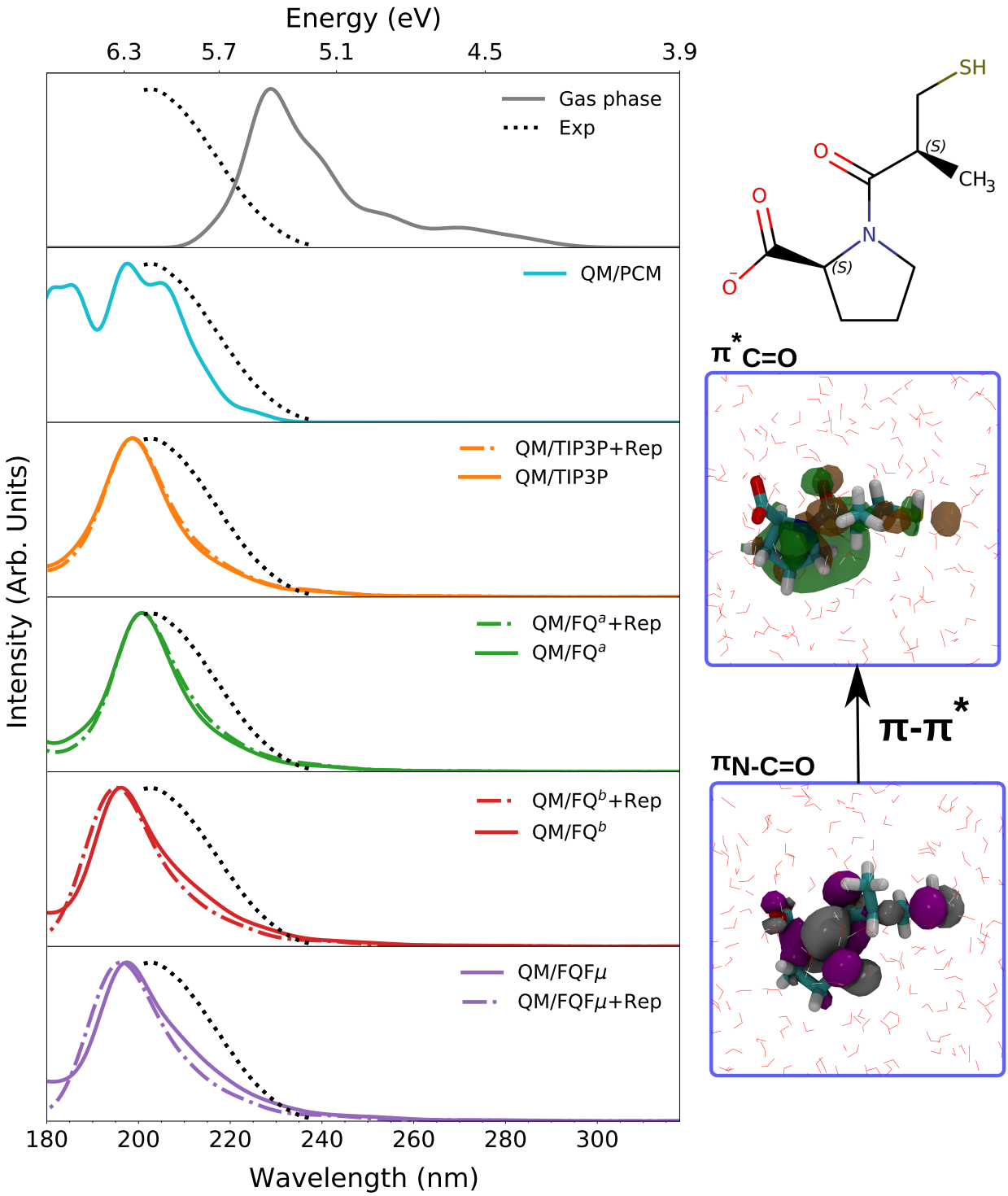

Figure 5: Left: UV-Vis spectra of (2S)-CAP at the CAM-B3LYP/aug-cc-pVDZ level of theory. Computed vacuum, QM/PCM, QM/TIP3P, QM/FQ^a, QM/FQ^b and QM/FQFμ spectra (with and without the inclusion of Pauli repulsion in the case of atomistic models) are reported. The experimental spectrum is adapted from Ref 80. Right: CAP Molecular Orbitals (MOs) involved in the main electronic transitions.

4.1.3 ECD Spectrum

We now move on to analyze the ECD spectrum of CAP in water. Fig. 6 shows the simulated ECD spectra of CAP at different levels of treatment of solvent effects. Such spectra result from convoluting raw data as those offered as an example in Fig. 4, top panel. The remaining ECD-stick spectra in Fig. S4 in the SI, plotted in the 150-320 nm interval, reveal that each approach offers a unique disposition of the sticks and the band broadening is automatically added because of the configurational variability which is achieved in the MD sampling. Also, it is worth noting that there is a higher complexity in the ECD spectra compared to UV/Vis, resulting from the sign alternation underlying each convoluted band. This is due to both conformational changes of the solute and the dynamical sampling of the surrounding water molecules and is typical for all chiroptical spectroscopies.[7,17] Even though ECD spectral patterns below 180 nm (see Fig. S4 in the SI) are different going from one approach to the other (see entirely positive (+) or alternating positive, negative, positive (+,-,+) features), the emergence of the prominent negative band at around 200 nm (Fig. 6), seems to be a general characteristic of convoluted spectra. As expected from the UV-Vis results, QM/FQ^b and QM/FQFμ spectra are somewhat similar, thus pointing out the marginal impact of adding fluctuating dipoles in the case of CAP ECD spectra.

According to Brittain and Kadin[80], CAP experimental ECD spectrum consists of a strong single negative peak located at 210 nm, which is confirmed by the recent measurements performed in water by Rahman and Khan[81], who found the same negative band centered at ≈208 nm. The measured ECD spectrum taken from Ref. 81 is also given in Fig. 6. In order to investigate the performance of the considered solvation models, Table S2 reports the position of the negative main band for both CAP and NAP (see below). As in the case of the UV-Vis absorption spectrum, modeling ECD for CAP in the gas phase fails at reproducing the experimental pattern, giving two negative peaks located far from 208 nm. In contrast, PCM and the non-polarizable TIP3P offer a small improvement in the position of the negative band, and the quality of the reproduction of experiments raises

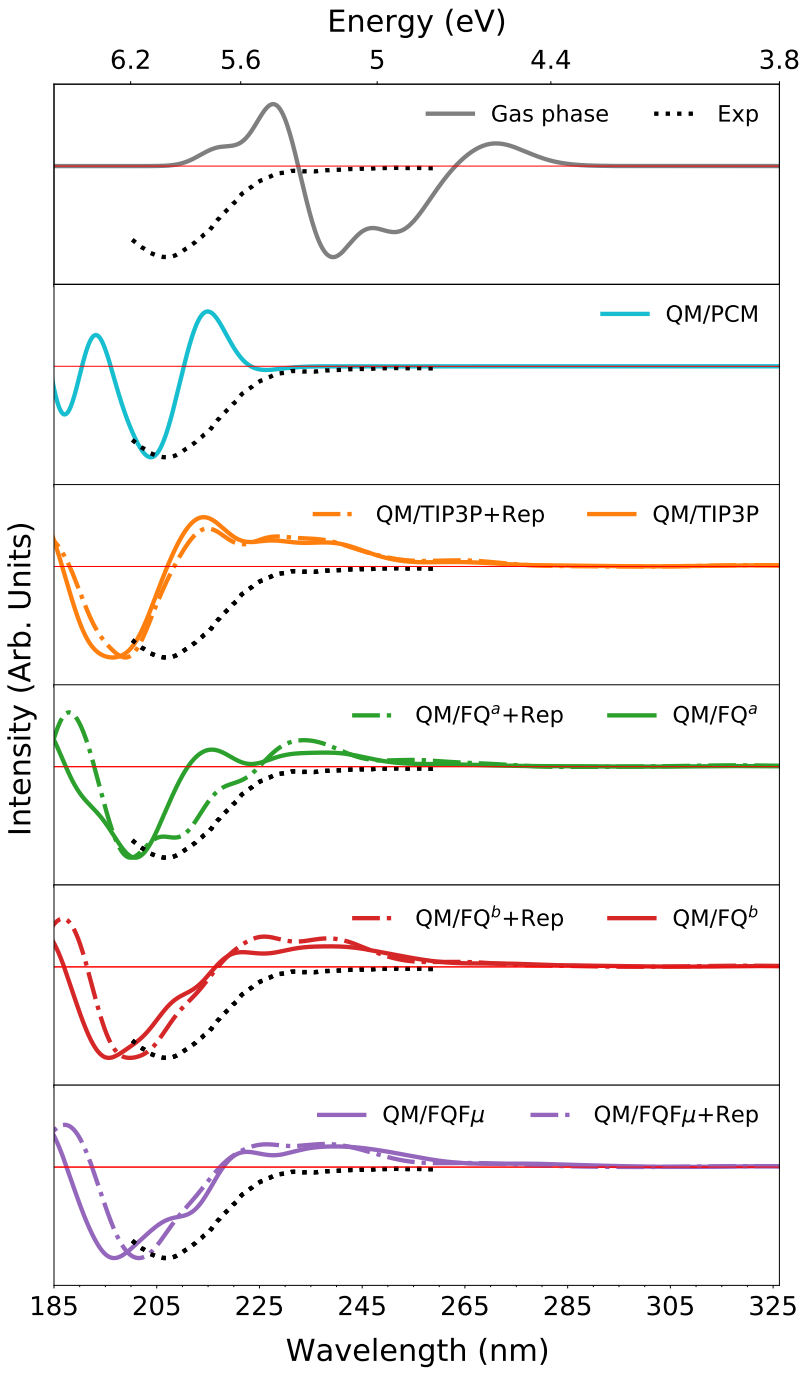

Figure 6: ECD spectra of (2S)–CAP at the CAM-B3LYP/aug-cc-pVDZ level of theory. Computed vacuum, QM/PCM, QM/TIP3P, QM/FQ^a, QM/FQ^b and QM/FQFμ spectra (with and without the inclusion of Pauli repulsion in the case of discrete models) are reported. The experimental spectrum is adapted from Ref 81.

even more when the polarizable QM/FQ and QM/FQFμ are employed, with the negative (-)–band peaking at 201 nm in the QM/FQ^a spectral profile. Focusing on the QM/FQ^a and QM/FQFμ spectra, we see that the inclusion of fluctuating dipoles in the MM portion, which increases the molecular dipole moment of MM water molecules, does not affect to a large extent the position of the main band. Differently, their effect can be better appreciated in the band broadening and the different sign alternation. However, when repulsion is considered, the results become closer to the experimental observations, due to the redshift of the bands and the different band broadening. Indeed, repulsion plays an opposite role for the ECD of solvated CAP compared to the effect in the absorption spectra (blue-shift). In addition, all QM/MM spectral profiles present a weak positive band right after 225 nm, of which intensity diminishes with the addition of extra snapshots, as can be seen in the convergence plots in the SI (Figs. S7 and S8). This observation confirms that the ECD spectrum is sensitive to diverse solute and solute-solvent conformations, which is reflected in the higher number of configurations needed to reach convergence when compared to UV–Vis.[17] Rahman and Khan[81] have proposed that the negative band at about 208 nm may be due to $n \rightarrow \pi^*$ transition of the carboxylate group mixed with the $n \rightarrow \sigma^*$ transition of the amino group of the proline moiety. Our analysis, based on the CMO decomposition, suggests that such a band is associated with a $\pi \rightarrow \pi^*$ transition.

4.1.4 NBO analysis

The improvement observed in both UV-Vis and ECD spectra when the solvent is treated atomistically reveals a role of HB interactions in the spectral behavior of the solute. Hence, it is important to analyze how strong CAP$\cdots$water interactions are. In our multiscale calculations, we resort to the NBO analysis quantifying the primary orbital overlapping in the cluster (CAP + explicit water molecules) while the remaining water molecules are described with the FQ^a model. Fig. 7a) depicts the eight water molecules more heavily interacting with CAP in a selected MD snapshot.

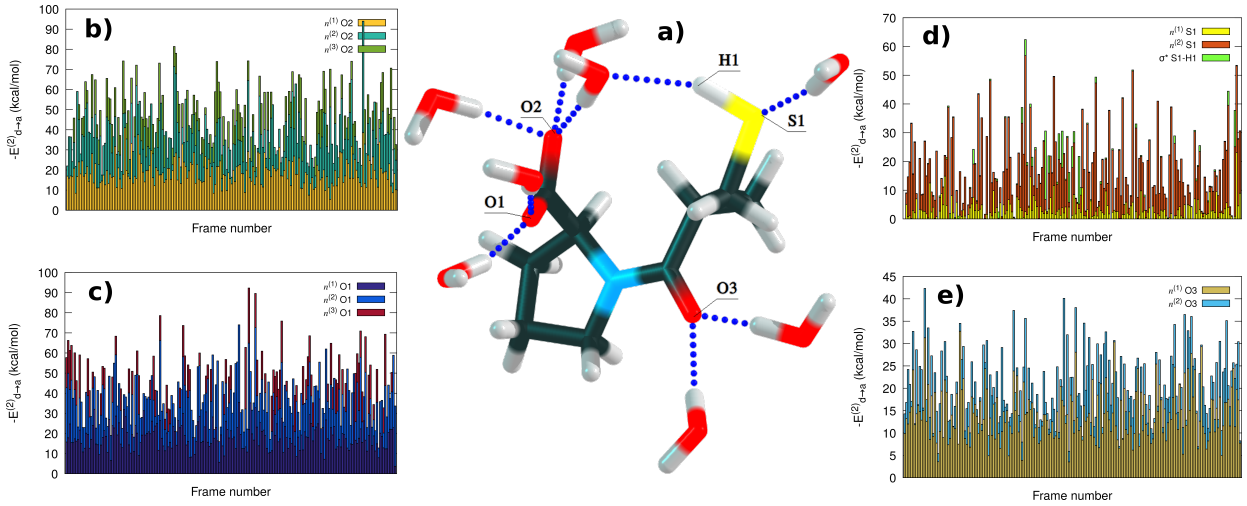

Figure 7: Closest water molecules to CAP in one of the MD snapshots (panel a) and evolution of the stabilization energies associated to the $n_{\mathrm{O_c}} \rightarrow \sigma^*_{\mathrm{H_w-O}}$ $\mathrm{O_c} = \mathrm{O1}, \mathrm{O2}, \mathrm{O3}$ charge transfers, panels b), c) y d), respectively, and $n_{\mathrm{S1}} \rightarrow \sigma^*_{\mathrm{H_w-O}}$, and $n_{\mathrm{O_w}} \rightarrow \sigma^*_{\mathrm{H-S}}$ charge transfers, panel e), along the entire MD simulation. In the stacked plots, the largest $|E^{(2)}_{\mathrm{d\rightarrow a}}|$ is used for each orbital interaction.

Orbital interactions responsible for maintaining solute-solvent, or CAP/water contacts, involve lone pairs (n) and antibonding (σ^*) orbitals and are of the $n_{\mathrm{O_c}} \rightarrow \sigma^*_{\mathrm{H_w-O}}$ $\mathrm{O_c} = \mathrm{O1}, \mathrm{O2}, \mathrm{O3}$, $n_{\mathrm{S1}} \rightarrow \sigma^*_{\mathrm{H_w-O}}$, and $n_{\mathrm{O_w}} \rightarrow \sigma^*_{\mathrm{H-S}}$ type. The stabilization resulting from those charge transfers is quantified in the different panels of Fig. 7. Although interactions with the solvent do not vary in nature during the MD simulations, water molecules are arranged distinctly on each snapshot, causing different interaction strengths (the higher the $|E^{(2)}_{\mathrm{d\rightarrow a}}|$ value, the stronger the interaction). Consequently, different oscillator and rotatory strengths are reported for each snapshot, resulting in a diverse broadening of the transition bands as shown in the previous sticks-like and convoluted spectra. Due to the nature of the carboxylate group, in some frames, a third lone pair appears in either O1 or O2 oxygen atoms. Those HBs are charge-assisted, and so they are stronger (maximum $-\sum E^{(2)}_{\mathrm{d\rightarrow a}} = 91$ kcal/mol) than those formed via the two lone pairs in O3 (maximum $-\sum E^{(2)}_{\mathrm{d\rightarrow a}} = 42$ kcal/mol). Similar values have been reported in the literature for systems with a carboxylate group mediating the interaction with the solvent.[71,82,83] Also, it should be noticed that the $n_{\mathrm{O_w}} \rightarrow \sigma^*_{\mathrm{H-S}}$ charge transfer, just once exceeding $-E^{(2)}_{\mathrm{d\rightarrow a}} = 20$ kcal/mol (see green bars in panel d) of Fig.

7), is found only in a few cases, because of the dynamical variability of the solute during the simulation that is certainly expected to affect the modeled spectra. The cumulative quantification of the strength of the main orbital interactions that keep CAP in contact with adjacent water molecules is displayed in Fig. S9 in the SI. Remarkably, frames with a large cumulative $|E^{(2)}_{\mathrm{d}\rightarrow\mathrm{a}}|$ have UV-Vis and ECD spectra more akin to the experiments.

4.2 (S)-Naproxen

4.2.1 Conformational, MD and NBO analysis

Structural analysis of neutral and anionic Naproxen has been previously done in multiple works.[84–86] Here, NAP conformers are first located by exploiting the implicit PCM model. Scan results at the CAM-B3LYP/aug-cc-pVDZ level of theory can be seen in Fig. S10 of SI. Individual δ_1 and δ_2 rotational barriers do not surpass 4 kcal/mol. Four different structures are found to be stable at this level of theory, as reported in Fig. 8(a). Overall, these conformations differ in the relative orientation of the carboxylate group with respect to the naphthalene moiety, as pointed out in earlier studies by Wenzel and Buss[84]. These structures are used in the subsequent gas phase and QM/PCM calculations and the results obtained are Boltzmann averaged. Motif **B**, that is the absolute minimum, is the initial structure for the MD runs.

Before discussing UV-Vis and ECD spectra of NAP in aqueous solution, we will examine the MD trajectory to gain insights into NAP conformers and the solvent local structure around them. Since the main conformational freedom of NAP stems from the δ_1 and δ_2 dihedral angles shown in Fig. 1, Fig. 8(b) compares the DDFs of these two angles as obtained from the MD runs, which have started from the lowest energy QM/PCM optimized structure. Two observations are to be stressed from that figure: (*i*) There is a good agreement between the configurations extracted from the MD and those obtained from the QM/PCM dihedral scan, which seem to be their centroids, (*ii*) in contrast to the few equilibrium structures

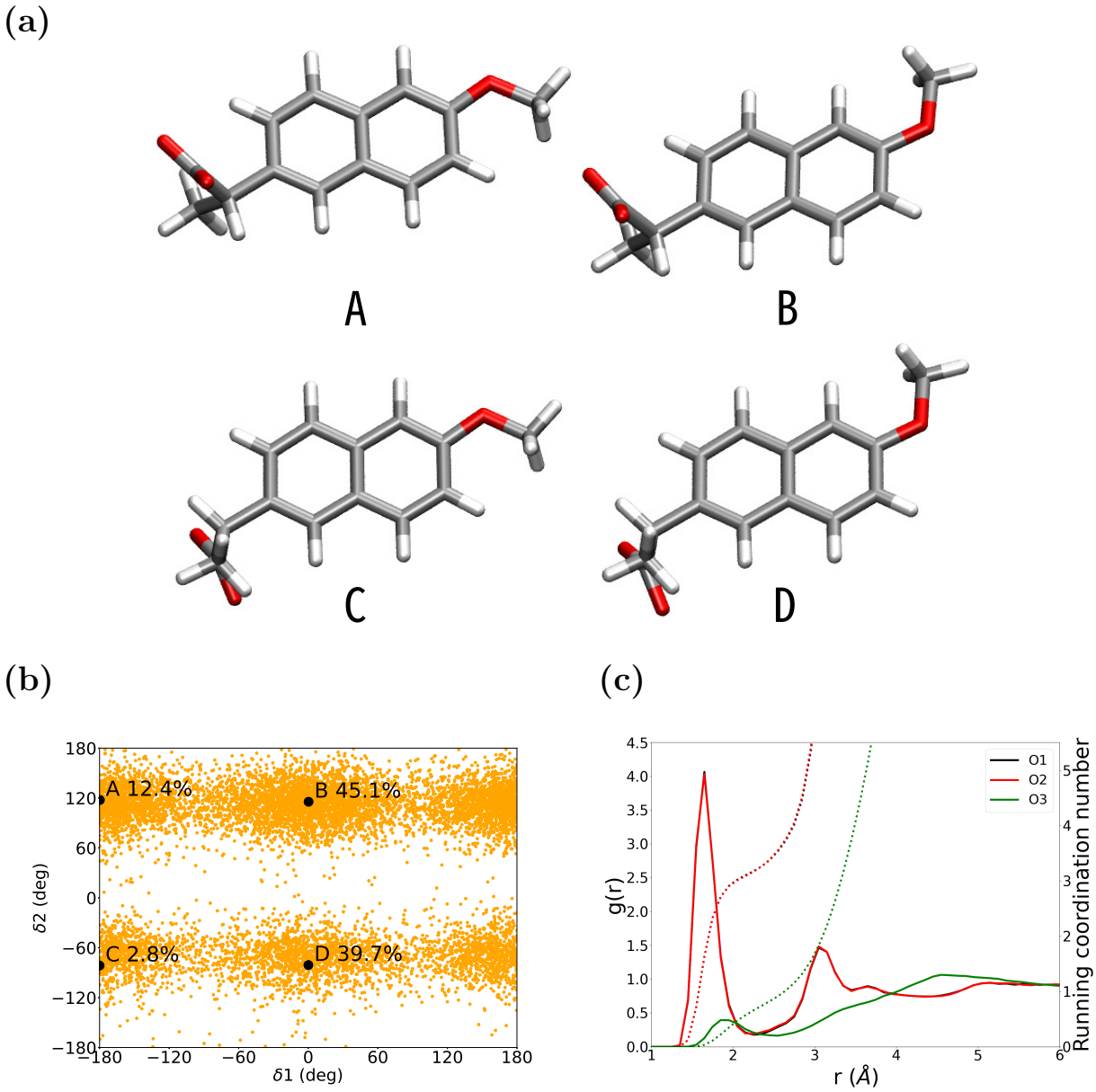

Figure 8: (a) NAP stable structures obtained from the dihedral scans (Figure S10) (b) Combined dihedral distribution function of $\delta 1$ and $\delta 2$ dihedral angles. (c) RDFs (continue lines) and RCNs (dotted lines) of NAP in aqueous solution. Labels are reported in Figure 1b.

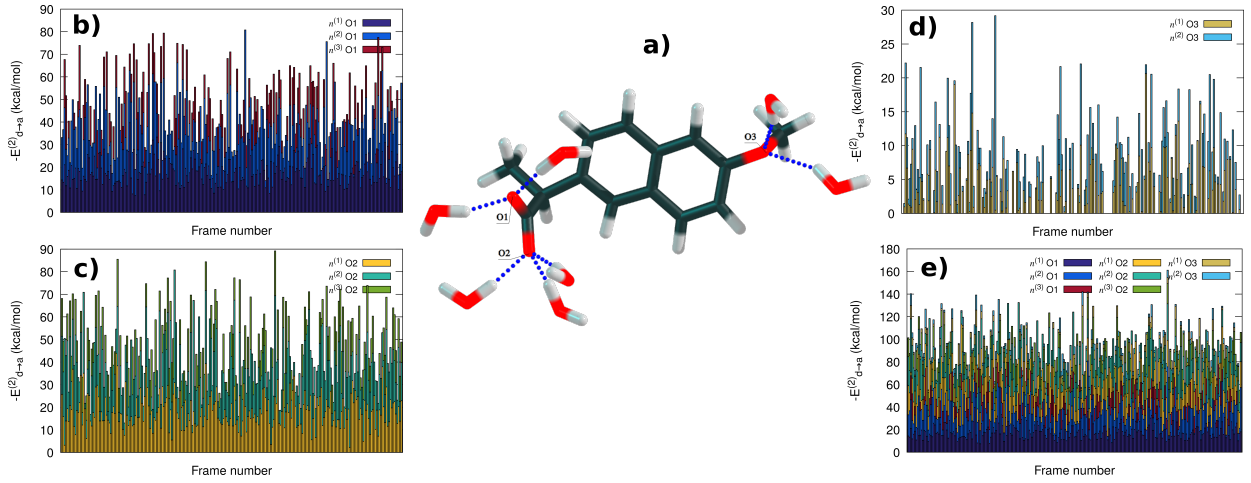

Figure 9: Closest water molecules to NAP in a selected MD snapshot (panel a) and evolution of the stabilization energies associated to the $n_{\mathrm{O_n}} \rightarrow \sigma^*_{\mathrm{H_w-O}}$ $\mathrm{O_n} = \mathrm{O1}, \mathrm{O2}, \mathrm{O3}$ charge transfers, panels b), c) y d), respectively, along the entire MD simulation. In the stacked plots, the largest $|E^{(2)}_{\mathrm{d}\rightarrow\mathrm{a}}|$ is used for each orbital interaction. The cumulative $-\sum E^{(2)}_{\mathrm{d}\rightarrow\mathrm{a}}$ for each frame is shown in panel e).

considered when using continuum models, explicit approaches handle several structures extracted from the MD run, which are in equilibrium with their own surrounding environment, thus providing a conformational wealth to the property under investigation.

Fig. 8(c) reports the RDFs of all the oxygen atoms of NAP together with the corresponding RCNs. A well-defined sharp peak at about 1.65 Å for both carboxylate oxygen atoms (O1, O2) evinces a strong charge-assisted HB interaction with surrounding water molecules in the first solvation shell. RCN values of 3.0 are obtained for those oxygen atoms. As expected, the methoxy oxygen of NAP (O3) is less prone to form strong HBs with the water molecules, because of its etheric nature (presence of the methyl group). Indeed, this oxygen atom $g(r)$ curve is characterized by a broad peak around 1.85 Å and a coordination number of approximately 0.9. These findings indicate that about seven water molecules are involved in HB interactions with the NAP solute in the first solvation shell.

Further characterization of the hydration patterns of NAP dissolved in water is done by analyzing the NBO in the corresponding HBs. In Fig. 9a) NAP and its closest solvent molecules (seven) are displayed for one of the snapshots. We recall here that in the NBO

calculations, NAP and those water molecules are explicitly included in the QM portion, whereas the rest of the environment is also considered explicitly but at the FQ^a level. As it was done for CAP, the strength of the NAP$\cdots$water interactions via the potential specific sites O1, O2, and O3 is reported in the panels of Fig. 9. The high and sharp peaks seen for O1 and O2 in the RDFs of Fig. 8(c) find support in the strong stabilization energies ($-\sum E^{(2)}_{\mathrm{d}\rightarrow\mathrm{a}}$ up to 89 kcal/mol) associated with the $n_{\mathrm{O_n}} \rightarrow \sigma^*_{\mathrm{H_w-O}}$ $\mathrm{O_n} = \mathrm{O1}, \mathrm{O2}$ charge transfers plotted in panels b) and c) of Fig. 9. However, the two bar distributions are not equivalent because of the defined separation of charge that NBO yields when dealing with charged groups as carboxylates.

Similarly, $n_{\mathrm{O_3}} \rightarrow \sigma^*_{\mathrm{H_w-O}}$ mild interaction in panel d) of Fig. 9, which corresponds to the wider and low $g(r)$ found for O3 (see Fig. 8(c), is not always appearing. This interaction represents at most the $\approx 18\%$ of the total stabilization energy gained by the system with the HB network in the first solvation shell as estimated from the cumulative plot in panel e) of Fig. 9.

A detailed discussion about the interactions of NAP with water molecules investigated by means of quantum descriptors, as well as its UV-Vis and ECD spectra in the aqueous phase, have recently been reported in the works by Rojas-Valencia et al.[83],[87] for the insertion of the drug into a model cell membrane. Next, we will go over our spectral findings using diverse environmental representations.

4.2.2 UV-Vis Absorption Spectrum

Following the computational protocol, the UV-Vis spectrum of solvated NAP is calculated by averaging the results over different sets of uncorrelated snapshots extracted from the MD run. In Fig. S11, calculated QM/MM UV-Vis raw data (sticks) from 600 snapshots are reported together with their Gaussian convolutions. The convergence of the computed spectra was reached by using 100 snapshots (see Figs. S13-S14 in the SI). Computed UV-Vis spectra are characterized by two main bands in the 150-350 nm range, independently of

the specific QM/MM approach that is exploited. The first band has a low intensity and is located at about 300 nm for all the QM/MM models. The second band, which is also the most intense of the whole spectrum, is located at about 216 nm in the case of QM/TIP3P, whereas it redshifts to 221 nm in the case of QM/FQ^a and to 224 nm for both QM/FQ^b and QM/FQFμ.

From a deeper inspection of Fig. S11, it can also be noticed that each QM/MM approach shows a peculiar spread in energies/wavelengths and intensities (sticks). This can be particularly appreciated by considering the larger spread reported by QM/FQ^b (and QM/FQFμ) with respect to QM/TIP3P and QM/FQ^a. Remarkably, by comparing QM/FQ and QM/FQFμ we observe that the mean contribution of the Fμs is small but not negligible because it affects the final spectral shape. In addition, when the electrostatic interaction is coupled with the Pauli repulsion term (see Fig. S11, right panels), the spread of the sticks is altered; this is not surprising, because the distortion of the QM density is the result of the presence of both the solvent molecules and the conformational changes of the QM portion itself, the two characteristics provided by the exhaustive sampling.

In Fig. 10 gas phase, QM/PCM and QM/MM UV-Vis spectra (900 frames) of NAP are presented together with the experimental spectrum,[85] which is reported as a dotted line. By comparing those spectra, it is observed that QM/PCM and QM/MM absorption spectra for CAP are very similar to each other, with a slight shift in the maximum wavelength. The gas phase spectrum is instead characterized by three main transitions, which are located at about 323, 268, and 252 nm, and thus completely differ with respect to all embedding approaches.

We finally move to compare computed and experimental results, which are taken from Ref. 85. Given the importance of NAP as a widely used nonsteroidal anti-inflammatory drug, its electronic absorption spectrum is well known and has been measured and simulated in different solvents.[84–90] Summarizing, the spectrum exhibits three main absorption bands in the 200-350 nm region: an intense and broad band with a maximum located at around

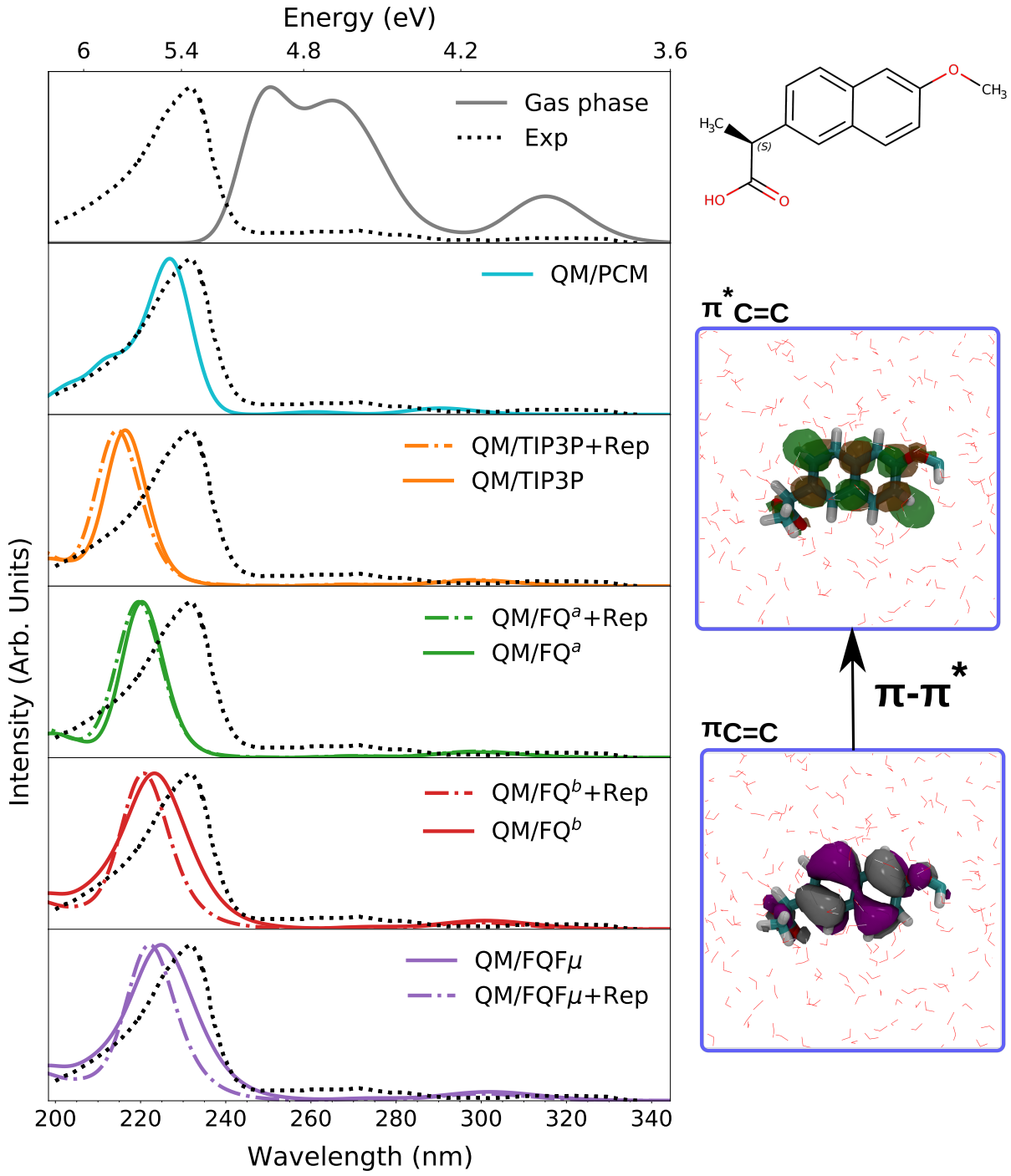

Figure 10: Left: UV-Vis spectra of (S)–NAP at the CAM-B3LYP/aug-cc-pVDZ level of theory. Computed vacuum, QM/PCM, QM/TIP3P, QM/FQ^a, QM/FQ^b and QM/FQFμ spectra (with and without the inclusion of Pauli repulsion in the case of discrete models) are reported. The experimental spectrum is reproduced from Ref 85. Right: NAP Molecular Orbitals (MOs) which are involved in the main electronic transitions.

230 nm (plus a shoulder at 215 nm) and two weak peaks at 270 and 320 nm.[88–90] The intensive absorbance at 230 nm features inhomogeneous band broadening, probably due to vibronic contributions. Studies have shown that the appearance of such absorption bands is practically independent of the solvent polarity, but there could be small shifts in their location.[85,90] By looking at Fig. 10, it can be noticed that both the bandshape and the relative intensities of the experimental UV-Vis spectra are well reproduced by using both continuum and explicit methods. All QM/MM models predict a blueshift for the most intense band, which is most exacerbated for the non-polarizable QM/TIP3P approach, and when Pauli repulsion is included (see Table S2 in the SI). All embedding approaches reproduce the additional weak band at about 320 nm.

For a better understanding of the absorption spectrum, the orbitals involved in the main transitions are analyzed. Such orbitals are graphically depicted on the right panel of Fig. 10. According to these plots and confirming previous assignments,[84,86,87] NAP absorptions at 310, 270, and 230 nm and the shoulder at 215 nm are essentially due to naphthalene excitations that are coupled to carboxylate transitions (mainly the $n \rightarrow \pi^*$ to lead the signals of the vibronic band system extending from 250 to 280 nm). They can be chiefly grouped in a $\pi \rightarrow \pi^*$ transition, as it is also supported by the CMO analysis. Overall, these orbitals correspond to HOMO, LUMO, and their immediate neighbors, independently of the solvation approach used in the calculations. Based on those orbital plots, the methoxy group linked to the naphthalene exerts only a minor perturbing effect.

4.2.3 ECD Spectrum

To model the ECD spectra of NAP in aqueous solution, 900 uncorrelated snapshots are extracted from the MD run (convergence tests are analyzed in Figs. S15-S16 in the SI). Requiring so many snapshots to reach a converged ECD spectrum highlights that, in contrast to UV/Vis absorption, ECD is highly dependent on molecular conformations and environmental effects. These findings are not surprising, in light of previous studies on chiroptical

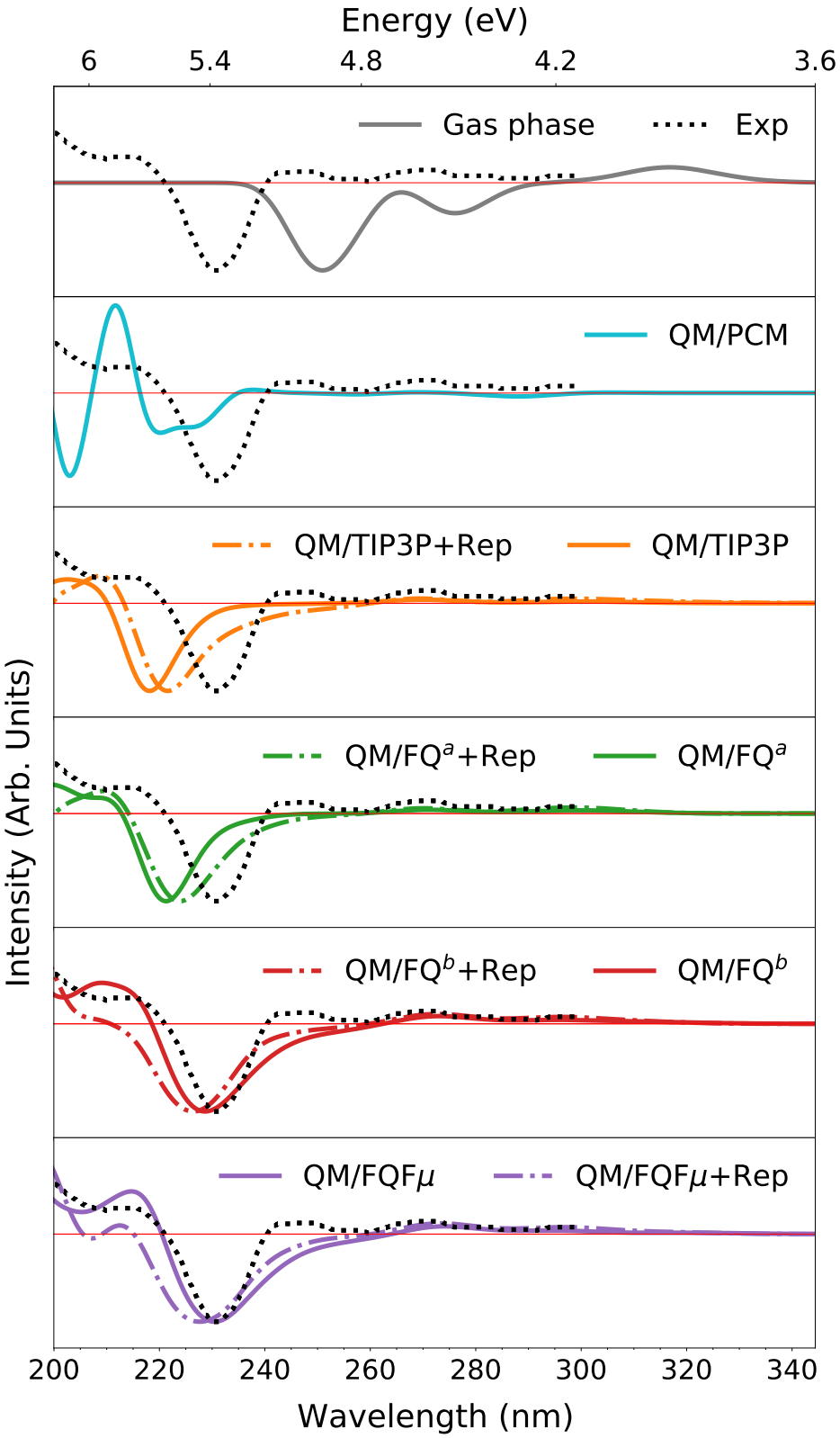

Figure 11: ECD spectra of (S)-NAP at the CAM-B3LYP/aug-cc-pVDZ level of theory. Computed vacuum, QM/PCM, QM/TIP3P, QM/FQ^a, QM/FQ^b and QM/FQFμ spectra (with and without the inclusion of Pauli repulsion in the case of discrete models) are reported. The experimental spectrum is reproduced from Ref 85. In the case of vacuum and QM/PCM, the Boltzmann weighted spectra are reported.

signals.[22,91–94]

In Fig. S12 in the SI QM/MM ECD raw data (sticks) are reported together with convoluted spectra. Each model shows a different spread of energies/wavelengths, intensities, and band broadening. The sign of the sticks varies with the snapshots because, in our model, the dynamic nature of the solute-solvent interactions and solute conformational changes are taken into consideration. From 200 nm on and independently of the QM/MM approach, each ECD spectrum is characterized by a well-defined negative band and weak positive bands. However, extra positive (also intense) bands can appear if the range of interest is extended (e.g., 150-350 nm see Fig. S12).

Fig. 11 shows computed vacuum, QM/PCM, and QM/MM ECD spectra along with the experiment.[85] Differently from QM/MM approaches, the calculated NAP ECD spectrum in the gas phase is characterized by two negative peaks in the 200-350 nm range. On the other hand, with an implicit description of the solvent (QM/PCM) six peaks are found, with a (-,+,-,+,+,+) sign pattern, while a single negative band dominates the spectral profile in the QM/MM approaches.

Next, we compare simulated and experimental spectra. The experimental ECD spectrum is characterized by a main negative band at about 230 nm and two weakly positive peaks at about 240 and 270 nm.[85] It has previously been reported that solvent effects profoundly impact the NAP ECD spectrum.[85] Indeed, the experimentally observed ECD signal inversion in the presence of ethanol and water when compared with polar aprotic solvents such as acetonitrile can be associated with the distinct contribution of different conformers of NAP.[85] Gas phase and QM/PCM approaches fail at reproducing the experimental pattern. Notwithstanding, results in the gas phase resemble a shifted spectrum. The discrepancy that is observed in the case of QM/PCM can be ascribed to the fact that only four conformers, each characterized by a specific spectral lineshape, are taken into account to obtain the final spectra. In contrast, many conformations are used in averaged QM/MM results (see Figs. S15-S16). As a consequence, the latter approaches produce spectra that are remarkably

in good agreement with the experiment, as outlined in Table S2. QM/FQ^b and QM/FQFμ better reproduce the experimental bandshape, particularly in the regions 200-220 nm and 260-300 nm. For these methods, the inclusion of Pauli repulsion yields a blueshift of the main band and an associated bandwidth increase.

5 Summary and conclusions

In this work, we have modeled and analyzed the UV-Vis and ECD spectra of two common chiral pharmaceutical molecules, namely anionic (2S)–Captopril and (S)-Naproxen in aqueous solution. We have studied the influence of the surrounding medium and of the conformational freedom on the spectra.

After conducting dihedral scans, we have identified four possible motifs or conformations for each solute. These conformations can easily be interconverted through single-bond rotations, with NAP having lower barriers. Since ECD is very sensitive to solute conformations and solvent effects, we have employed Molecular Dynamics (MD) and sampled wide regions of the configurational space. We have found that the final ECD spectra are deeply influenced by the conformational flexibility of the molecules and the surrounding water molecules because, unlike absorption spectra, which only require 100 snapshots to converge, ECD spectra need 900 configurations to achieve convergence.

To test their performance, the QM/PCM and four multiscale approaches (QM/FQ^a, QM/FQ^b, QM/FQFμ, and QM/TIP3P) have been compared with experimentally recorded spectra. The main bands characterizing the two kinds of spectra stem from $\pi \rightarrow \pi^*$ transitions. Our results also indicate that despite the variability in energies and intensities, for both CAP and NAP, UV-Vis QM/MM results are comparable with QM/PCM, and all agree with the experiment. The inclusion of Pauli repulsion exerts only a minor, almost imperceptible effect on spectra. On the contrary, for ECD the implicit QM/PCM approach alters the ECD patterns of the solutes, whereas QM/MM findings are much closer to experimen-

tal measurements. This emphasizes that MD sampling becomes fundamental to correctly reproducing ECD features. Also, the inclusion of Pauli repulsion modifies band broadening. Finally, even if slight shifts can be seen, the agreement with the experimental results is best reported for QM/FQFμ. We have further shown that for the studied systems, there are strong interactions with the near water molecules; this is the reason why atomistic models are required to represent the aqueous environment. The outcomes presented here demonstrate that electronic spectroscopic signatures can be accurately investigated, provided that a reliable computational protocol is applied.

Acknowledgement

We gratefully acknowledge the Center for High-Performance Computing (CHPC) at SNS for providing the computational infrastructure. CC acknowledges the support of the European Union by the Next Generation EU project ECS00000017 'Ecosistema dell'Innovazione' Tuscany Health Ecosystem (THE, PNRR, Spoke 4: Nanotechnologies for diagnosis and therapy).

Supporting Information Available

Additional plots for conformational analyses, sticks-like spectra, convergence plots, and NBO analysis.

References

(1) Warnke, I.; Furche, F. Circular dichroism: electronic. *Wiley Interdiscip. Rev. Comput. Mol. Sci.* **2012**, *2*, 150–166.

(2) Berova, N.; Nakanishi, K.; Woody, R. *Circular Dichroism: Principles and Applications*; Wiley, 2000.

(3) Berova, N.; Polavarapu, P. L.; Nakanishi, K.; Woody, R. W. *Comprehensive Chiroptical Spectroscopy, Volume 2: Applications in Stereochemical Analysis of Synthetic Compounds, Natural Products, and Biomolecules*; John Wiley & Sons, 2012; Vol. 2.

(4) Nafie, L. *Vibrational Optical Activity: Principles and Applications*; Wiley, 2011.

(5) Nafie, L. A. Vibrational optical activity: From discovery and development to future challenges. *Chirality* **2020**, *32*, 667–692.

(6) Giovannini, T.; Del Frate, G.; Lafiosca, P.; Cappelli, C. Effective computational route towards vibrational optical activity spectra of chiral molecules in aqueous solution. *Phys. Chem. Chem. Phys.* **2018**, *20*, 9181–9197.

(7) Sepali, C.; Lafiosca, P.; Gómez, S.; Giovannini, T.; Cappelli, C. Effective fully polarizable QM/MM approaches to compute Raman and Raman Optical Activity spectra in aqueous solution. *Spectrochim. Acta A Mol. Biomol. Spectrosc.* **2024**, *305*, 123485.

(8) Edwards, A.; Jenkinson, S. In *Comprehensive Chirality*; Carreira, E. M., Yamamoto, H., Eds.; Elsevier: Amsterdam, 2012; pp 39–53.

(9) Kuball, H.-G.; Höfer, T.; Kiesewalter, S. In *Encyclopedia of Spectroscopy and Spectrometry (Third Edition)*, third edition ed.; Lindon, J. C., Tranter, G. E., Koppenaal, D. W., Eds.; Academic Press: Oxford, 2017; pp 217–231.

(10) Berova, N.; Di Bari, L.; Pescitelli, G. Application of electronic circular dichroism in configurational and conformational analysis of organic compounds. *Chem. Soc. Rev.* **2007**, *36*, 914–931.

(11) Pescitelli, G.; Di Bari, L.; Berova, N. Application of electronic circular dichroism in the study of supramolecular systems. *Chem. Soc. Rev.* **2014**, *43*, 5211–5233.

(12) Siligardi, G.; Hussain, R. In *Encyclopedia of Spectroscopy and Spectrometry (Third*

Edition), third edition ed.; Lindon, J. C., Tranter, G. E., Koppenaal, D. W., Eds.; Academic Press: Oxford, 2017; pp 293–298.

(13) Zhu, S.; Sun, M. Electronic circular dichroism and raman optical activity: principle and applications. *Appl. Spectrosc. Rev.* **2021**, *56*, 553–587.

(14) Egidi, F.; Russo, R.; Carnimeo, I.; D'Urso, A.; Mancini, G.; Cappelli, C. The electronic circular dichroism of nicotine in aqueous solution: a test case for continuum and mixed explicit-continuum solvation approaches. *J. Phys. Chem. A* **2015**, *119*, 5396–5404.

(15) Gorelsky, S. In *Encyclopedia of Spectroscopy and Spectrometry (Third Edition)*, third edition ed.; Lindon, J. C., Tranter, G. E., Koppenaal, D. W., Eds.; Academic Press: Oxford, 2017; pp 447–451.

(16) Monti, M.; Stener, M.; Aschi, M. A computational approach for modeling electronic circular dichroism of solvated chromophores. *J. Comput. Chem.* **2022**, *43*, 2023–2036.

(17) Giovannini, T.; Egidi, F.; Cappelli, C. Theory and algorithms for chiroptical properties and spectroscopies of aqueous systems. *Phys. Chem. Chem. Phys.* **2020**, *22*, 22864–22879.

(18) Bredehöft, J. H.; Jones, N. C.; Meinert, C.; Evans, A. C.; Hoffmann, S. V.; Meierhenrich, U. J. Understanding photochirogenesis: Solvent effects on circular dichroism and anisotropy spectroscopy. *Chirality* **2014**, *26*, 373–378.

(19) Senn, H. M.; Thiel, W. QM/MM methods for biomolecular systems. *Angewd. Chem. Int. Ed.* **2009**, *48*, 1198–1229.

(20) Giovannini, T.; Cappelli, C. Continuum vs. atomistic approaches to computational spectroscopy of solvated systems. *ChemComm* **2023**, *59*, 5644–5660.

(21) Giovannini, T.; Egidi, F.; Cappelli, C. Molecular spectroscopy of aqueous solutions: a theoretical perspective. *Chem. Soc. Rev.* **2020**, *49*, 5664–5677.

(22) Nørby, M. S.; Olsen, J. M. H.; Steinmann, C.; Kongsted, J. Modeling electronic circular dichroism within the polarizable embedding approach. *J. Chem. Theory Comput.* **2017**, *13*, 4442–4451.

(23) Steinmann, C.; Reinholdt, P.; Nørby, M. S.; Kongsted, J.; Olsen, J. M. H. Response properties of embedded molecules through the polarizable embedding model. *Int. J. Quantum Chem.* **2019**, *119*, e25717.

(24) Cappelli, C. Integrated QM/polarizable MM/continuum approaches to model chiroptical properties of strongly interacting solute–solvent systems. *Int. J. Quantum Chem.* **2016**, *116*, 1532–1542.

(25) Nicoli, L.; Giovannini, T.; Cappelli, C. Assessing the quality of QM/MM approaches to describe vacuo-to-water solvatochromic shifts. *J. Chem. Phys.* **2022**, *157*, 214101.

(26) Giovannini, T.; Puglisi, A.; Ambrosetti, M.; Cappelli, C. Polarizable QM/MM Approach with Fluctuating Charges and Fluctuating Dipoles: The QM/FQFμ Model. *J. Chem. Theory Comput.* **2019**, *15*, 2233–2245.

(27) Giovannini, T.; Riso, R. R.; Ambrosetti, M.; Puglisi, A.; Cappelli, C. Electronic transitions for a fully polarizable qm/mm approach based on fluctuating charges and fluctuating dipoles: linear and corrected linear response regimes. *J. Chem. Phys.* **2019**, *151*, 174104.

(28) Giovannini, T.; Grazioli, L.; Ambrosetti, M.; Cappelli, C. Calculation of ir spectra with a fully polarizable qm/mm approach based on fluctuating charges and fluctuating dipoles. *J. Chem. Theory Comput.* **2019**, *15*, 5495–5507.

(29) Puglisi, A.; Giovannini, T.; Antonov, L.; Cappelli, C. Interplay between conformational and solvent effects in UV-visible absorption spectra: Curcumin tautomers as a case study. *Phys. Chem. Chem. Phys.* **2019**, *21*, 15504–15514.

(30) Giovannini, T.; Macchiagodena, M.; Ambrosetti, M.; Puglisi, A.; Lafiosca, P.; Lo Gerfo, G.; Egidi, F.; Cappelli, C. Simulating vertical excitation energies of solvated dyes: From continuum to polarizable discrete modeling. *Int. J. Quantum Chem.* **2019**, *119*, e25684.

(31) Giovannini, T.; Lafiosca, P.; Cappelli, C. A general route to include Pauli repulsion and quantum dispersion effects in QM/MM approaches. *J. Chem. Theory Comput.* **2017**, *13*, 4854–4870.

(32) Giovannini, T.; Lafiosca, P.; Chandramouli, B.; Barone, V.; Cappelli, C. Effective yet reliable computation of hyperfine coupling constants in solution by a QM/MM approach: Interplay between electrostatics and non-electrostatic effects. *J. Chem. Phys.* **2019**, *150*, 124102.

(33) Giovannini, T.; Ambrosetti, M.; Cappelli, C. Quantum Confinement Effects on Solvatochromic Shifts of Molecular Solutes. *J. Phys. Chem. Lett.* **2019**, *10*, 5823–5829.

(34) Marrazzini, G.; Giovannini, T.; Egidi, F.; Cappelli, C. Calculation of linear and nonlinear electric response properties of systems in aqueous solution: A polarizable quantum/classical approach with quantum repulsion effects. *J. Chem. Theory Comput.* **2020**, *16*, 6993–7004.

(35) Ambrosetti, M.; Skoko, S.; Giovannini, T.; Cappelli, C. Quantum mechanics/fluctuating charge protocol to compute solvatochromic shifts. *J. Chem. Theory Comput.* **2021**, *17*, 7146–7156.

(36) Giovannini, T.; Lafiosca, P.; Cappelli, C. A General Route to Include Pauli Repulsion and Quantum Dispersion Effects in QM/MM Approaches. *J. Chem. Theory Comput.* **2017**, *13*, 4854–4870.

(37) Remko, M.; Bojarska, J.; Remková, A.; Maniukiewicz, W. Molecular structure and

acidity of captopril, zofenopril and their metabolites captopril disulfide and zofenoprilat. *Comput. Theor. Chem* **2015**, *1062*, 50–55.

(38) Kean, W. F.; Lock, C. J.; Rischke, J.; Butt, R.; Buchanan, W. W.; Howard-Lock, H. Effect of R and S enantiomers of naproxen on aggregation and thromboxane production in human platelets. *J. Pharm. Sci.* **1989**, *78*, 324–327.

(39) Ragab, M. A.; Eman, I. High performance liquid chromatography with photo diode array for separation and analysis of naproxen and esomeprazole in presence of their chiral impurities: enantiomeric purity determination in tablets. *J. Chromatogr. A* **2017**, *1497*, 110–117.

(40) Mayer, A. Formulation in terms of normalized propagators of a charge-dipole model enabling the calculation of the polarization properties of fullerenes and carbon nanotubes. *Phys. Rev. B* **2007**, *75*, 045407.

(41) Gómez, S.; Giovannini, T.; Cappelli, C. Multiple Facets of Modeling Electronic Absorption Spectra of Systems in Solution. *ACS Phys. Chem. Au.* **2023**, *3*, 1–16.

(42) Marques, M. *Time-Dependent Density Functional Theory*; Lecture Notes in Physics; Springer, 2006.

(43) Casida, M. E. In *Recent Advances in Density Functional Methods Part I*; Chong, D. P., Ed.; World Scientific, Singapore, 1995; pp 155–192.

(44) Norman, P.; Ruud, K.; Saue, T. *Principles and Practices of Molecular Properties: Theory, Modeling, and Simulations*; John Wiley & Sons, 2018.

(45) Marvin, Calculator Plugins were used for structure property prediction and calculation, Marvin 19.20, 2019, ChemAxon (http://www.chemaxon.com). 2019; `http://www.chemaxon.com/marvin`, Accessed Jun. 25, 2023.

(46) Duggan, K. C.; Walters, M. J.; Musee, J.; Harp, J. M.; Kiefer, J. R.; Oates, J. A.; Marnett, L. J. Molecular basis for cyclooxygenase inhibition by the non-steroidal anti-inflammatory drug naproxen. *J. Biol. Chem.* **2010**, *285*, 34950–34959.

(47) Akif, M.; Georgiadis, D.; Mahajan, A.; Dive, V.; Sturrock, E. D.; Isaac, R. E.; Acharya, K. R. High-resolution crystal structures of Drosophila melanogaster angiotensin-converting enzyme in complex with novel inhibitors and antihypertensive drugs. *J. Mol. Biol.* **2010**, *400*, 502–517.

(48) Tomasi, J.; Mennucci, B.; Cammi, R. Quantum mechanical continuum solvation models. *Chem. Rev.* **2005**, *105*, 2999–3094.

(49) Wang, J.; Wang, W.; Kollman, P. A.; Case, D. A. Automatic atom type and bond type perception in molecular mechanical calculations. *J. Mol. Graph. Model.* **2006**, *25*, 247–260.

(50) Wang, J.; Wolf, R. M.; Caldwell, J. W.; Kollman, P. A.; Case, D. A. Development and testing of a general amber force field. *J. Comput. Chem.* **2004**, *25*, 1157–1174.

(51) Cieplak, P.; Cornell, W. D.; Bayly, C.; Kollman, P. A. Application of the multimolecule and multiconformational RESP methodology to biopolymers: Charge derivation for DNA, RNA, and proteins. *J. Comput. Chem.* **1995**, *16*, 1357–1377.

(52) Wang, L.-P.; Martinez, T. J.; Pande, V. S. Building force fields: An automatic, systematic, and reproducible approach. *J. Phys. Chem. Lett.* **2014**, *5*, 1885–1891.

(53) Bussi, G.; Donadio, D.; Parrinello, M. Canonical sampling through velocity rescaling. *J. Chem. Phys.* **2007**, *126*, 014101.

(54) Parrinello, M.; Rahman, A. Polymorphic transitions in single crystals: A new molecular dynamics method. *J. Appl. Phys.* **1981**, *52*, 7182–7190.

(55) Darden, T.; York, D.; Pedersen, L. Particle mesh Ewald: An Nlog(N) method for Ewald sums in large systems. *J. Chem. Phys.* **1993**, *98*, 10089–10092.

(56) Essmann, U.; Perera, L.; Berkowitz, M. L.; Darden, T.; Lee, H.; Pedersen, L. G. A smooth particle mesh Ewald method. *J. Chem. Phys.* **1995**, *103*, 8577–8593.

(57) Hess, B.; Bekker, H.; Berendsen, H. J.; Fraaije, J. G. LINCS: a linear constraint solver for molecular simulations. *J. Comput. Chem.* **1997**, *18*, 1463–1472.

(58) Hess, B. P-LINCS: A parallel linear constraint solver for molecular simulation. *J. Chem. Theory Comput.* **2008**, *4*, 116–122.

(59) Bekker, H.; Berendsen, H.; Dijkstra, E.; Achterop, S.; von Drumen, R.; Van der Spoel, D.; Sijbers, A.; Keegstra, H.; Renardus, M. Gromacs: A parallel computer for molecular dynamics simulations. Physics computing '92. 1993; pp 252–256, 4th International Conference on Computational Physics (PC 92) ; Conference date: 24-08-1992 Through 28-08-1992.

(60) Berendsen, H. J.; van der Spoel, D.; van Drunen, R. GROMACS: A message-passing parallel molecular dynamics implementation. *Comput. Phys. Commun.* **1995**, *91*, 43–56.

(61) Lindahl, E.; Hess, B.; Van Der Spoel, D. GROMACS 3.0: a package for molecular simulation and trajectory analysis. *J. Mol. Model.* **2001**, *7*, 306–317.

(62) Van Der Spoel, D.; Lindahl, E.; Hess, B.; Groenhof, G.; Mark, A. E.; Berendsen, H. J. GROMACS: fast, flexible, and free. *J. Comput. Chem* **2005**, *26*, 1701–1718.

(63) Hess, B.; Kutzner, C.; Van Der Spoel, D.; Lindahl, E. GROMACS 4: algorithms for highly efficient, load-balanced, and scalable molecular simulation. *J. Chem. Theory Comput.* **2008**, *4*, 435–447.

(64) Pronk, S.; Páll, S.; Schulz, R.; Larsson, P.; Bjelkmar, P.; Apostolov, R.; Shirts, M. R.; Smith, J. C.; Kasson, P. M.; Van Der Spoel, D., et al. GROMACS 4.5: a high-throughput and highly parallel open source molecular simulation toolkit. *Bioinformatics* **2013**, *29*, 845–854.

(65) Brehm, M.; Kirchner, B. TRAVIS - A Free Analyzer and Visualizer for Monte Carlo and Molecular Dynamics Trajectories. *J. Chem. Inf. Model* **2011**, *51*, 2007–2023.

(66) Brehm, M.; Thomas, M.; Gehrke, S.; Kirchner, B. TRAVIS—A free analyzer for trajectories from molecular simulation. *J. Chem. Phys.* **2020**, *152*, 164105.

(67) Rick, S. W.; Stuart, S. J.; Berne, B. J. Dynamical fluctuating charge force fields: Application to liquid water. *J. Chem. Phys.* **1994**, *101*, 6141–6156.

(68) Reed, A. E.; Curtiss, L. A.; Weinhold, F. Intermolecular interactions from a natural bond orbital, donor-acceptor viewpoint. *Chem. Rev.* **1988**, *88*, 899–926.

(69) Weinhold, F.; Landis, C.; Glendening, E. What is NBO analysis and how is it useful? *Int. Rev. Phys. Chem.* **2016**, *35*, 399–440.

(70) Weinhold, F.; Landis, C. R. *Discovering Chemistry with Natural Bond Orbitals*; Wiley-VCH, Hoboken NJ, 319pp, 2012.

(71) Gómez, S.; Rojas-Valencia, N.; Giovannini, T.; Restrepo, A.; Cappelli, C. Ring Vibrations to Sense Anionic Ibuprofen in Aqueous Solution as Revealed by Resonance Raman. *Molecules* **2022**, *27*, 442.

(72) Gómez, S.; Giovannini, T.; Cappelli, C. Absorption spectra of xanthines in aqueous solution: A computational study. *Phys. Chem. Chem. Phys.* **2020**, *22*, 5929–5941.

(73) Uribe, L.; Gómez, S.; Giovannini, T.; Egidi, F.; Restrepo, A. An efficient and robust procedure to calculate absorption spectra of aqueous charged species applied to NO 2-. *Phys. Chem. Chem. Phys.* **2021**, *23*, 14857–14872.

(74) Frisch, M. J.; Trucks, G. W.; Schlegel, H. B.; Scuseria, G. E.; Robb, M. A.; Cheeseman, J. R.; Scalmani, G.; Barone, V.; Petersson, G. A.; Nakatsuji, H. et al. Gaussian 16 Revision A.03. 2016; Gaussian Inc. Wallingford CT.

(75) Glendening, E. D.; Badenhoop, J. K.; Reed, A. E.; Carpenter, J. E.; Bohmann, J. A.; Morales, C. M.; Karafiloglou, P.; Landis, C. R.; Weinhold, F. NBO 7.0. 2018; Theoretical Chemistry Institute, University of Wisconsin, Madison, WI.

(76) Mark, P.; Nilsson, L. Structure and dynamics of the TIP3P, SPC, and SPC/E water models at 298 K. *J. Phys. Chem. A* **2001**, *105*, 9954–9960.

(77) Luke, B. T. A quantum mechanical conformational search of captopril, a potent inhibitor of the angiotensin-converting enzyme. *J. Mol. Struct.: THEOCHEM* **1994**, *309*, 1–11.

(78) Zamarbide, G. N.; Estrada, M. R.; Zamora, M. A.; Torday, L. L.; Enriz, R. D.; Vert, F. T.; Csizmadia, I. G. An ab initio conformational study on captopril. *J. Mol. Struct.: THEOCHEM* **2003**, *666*, 599–608.

(79) Klamt, A.; Schüürmann, G. COSMO: a new approach to dielectric screening in solvents with explicit expressions for the screening energy and its gradient. *J. Chem. Soc., Perkin trans. II* **1993**, 799–805.

(80) Brittain, H. G.; Kadin, H. Ultraviolet (UV) absorption and circular dichroism (CD) spectra of captopril. *Pharm. Res.* **1990**, *7*, 1082–1085.

(81) Rahman, N.; Khan, S. Circular dichroism spectroscopy: A facile approach for quantitative analysis of captopril and study of its degradation. *ACS omega* **2019**, *4*, 4252–4258.

(82) Rojas-Valencia, N.; Gómez, S.; Montillo, S.; Manrique-Moreno, M.; Cappelli, C.; Hadad, C.; Restrepo, A. Evolution of bonding during the insertion of anionic ibuprofen into model cell membranes. *J. Phys. Chem. B* **2019**, *124*, 79–90.

(83) Rojas-Valencia, N.; Gómez, S.; Núñez-Zarur, F.; Cappelli, C.; Hadad, C.; Restrepo, A. Thermodynamics and intermolecular interactions during the insertion of anionic naproxen into model cell membranes. *J. Phys. Chem. B* **2021**, *125*, 10383–10391.

(84) Wenzel, S.; Buss, V. Circular dichroism and electronic structure calculations on naproxen. *J. Phys. Org. Chem.* **1992**, *5*, 748–754.

(85) Ximenes, V. F.; Morgon, N. H.; Robinson de Souza, A. Solvent-dependent inversion of circular dichroism signal in naproxen: An unusual effect! *Chirality* **2018**, *30*, 1049–1053.

(86) Saji, R. S.; Prasana, J. C.; Muthu, S.; George, J.; Kuruvilla, T. K.; Raajaraman, B. Spectroscopic and quantum computational study on naproxen sodium. *Spectrochim. Acta - A: Mol. Biomol. Spectrosc.* **2020**, *226*, 117614.

(87) Rojas-Valencia, N.; Gómez, S.; Giovannini, T.; Cappelli, C.; Restrepo, A.; Núñez-Zarur, F. Water Maintains the UV–Vis Spectral Features During the Insertion of Anionic Naproxen and Ibuprofen into Model Cell Membranes. *J. Phys. Chem. B* **2023**, *127*, 2146–2155.

(88) Fernandes, E.; Soares, T. B.; Gonçalves, H.; Lúcio, M. Spectroscopic studies as a toolbox for biophysical and chemical characterization of lipid-based nanotherapeutics. *Front. Chem.* **2018**, *6*, 323.

(89) Arany, E.; Szabó, R. K.; Apáti, L.; Alapi, T.; Ilisz, I.; Mazellier, P.; Dombi, A.; Gajda-Schrantz, K. Degradation of naproxen by UV, VUV photolysis and their combination. *J. Hazard. Mater.* **2013**, *262*, 151–157.

(90) Miotke, M. M.; Józefowicz, M. Solvatochromism of antiinflammatory drug–naproxen sodium. *J. Mol. Liq.* **2017**, *230*, 129–136.

(91) Lipparini, F.; Egidi, F.; Cappelli, C.; Barone, V. The optical rotation of methyloxirane in aqueous solution: a never ending story? *J. Chem. Theory Comput.* **2013**, *9*, 1880–1884.

(92) Egidi, F.; Giovannini, T.; Del Frate, G.; Lemler, P. M.; Vaccaro, P. H.; Cappelli, C. A combined experimental and theoretical study of optical rotatory dispersion for (R)-glycidyl methyl ether in aqueous solution. *Phys. Chem. Chem. Phys.* **2019**, *21*, 3644–3655.

(93) Giovannini, T.; Olszowka, M.; Cappelli, C. Effective fully polarizable QM/MM approach to model vibrational circular dichroism spectra of systems in aqueous solution. *J. Chem. Theory Comput.* **2016**, *12*, 5483–5492.

(94) Giovannini, T.; Olszowka, M.; Egidi, F.; Cheeseman, J. R.; Scalmani, G.; Cappelli, C. Polarizable embedding approach for the analytical calculation of Raman and Raman optical activity spectra of solvated systems. *J. Chem. Theory Comput.* **2017**, *13*, 4421–4435.

TOC Graphic

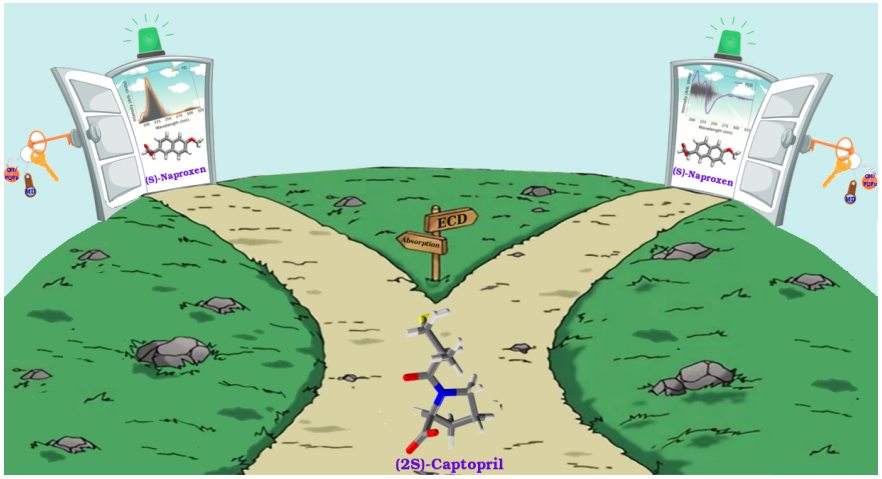

In aqueous solution, (2S)-Captopril and (S)-Naproxen establish strong contacts with solvent molecules via hydrogen bonds and such specific interactions play a major role in their UV-Vis and ECD spectral response.